

This work has been submitted to the IEEE for possible publication. Copyright may be transferred without notice, after which this version may no longer be accessible.

A Multi-Task Foundation Model for Wireless Channel Representation Using Contrastive and Masked Autoencoder Learning

Berkay Guler, Giovanni Geraci, and Hamid Jafarkhani

Abstract—Current applications of self-supervised learning to wireless channel representation often borrow paradigms developed for text and image processing, without fully addressing the unique characteristics and constraints of wireless communications. Aiming to fill this gap, we first propose WiMAE (Wireless Masked Autoencoder), a transformer-based encoder-decoder foundation model pretrained on a realistic open-source multi-antenna wireless channel dataset. Building upon this foundation, we develop ContraWiMAE, which enhances WiMAE by incorporating a contrastive learning objective alongside the reconstruction task in a unified multi-task framework. By warm-starting from pretrained WiMAE weights and generating positive pairs via noise injection, the contrastive component enables the model to capture both structural and discriminative features, enhancing representation quality beyond what reconstruction alone can achieve. Through extensive evaluation on unseen scenarios, we demonstrate the effectiveness of both approaches across multiple downstream tasks, with ContraWiMAE showing further improvements in linear separability and adaptability in diverse wireless environments. Comparative evaluations against a state-of-the-art wireless channel foundation model confirm the superior performance and data efficiency of our models, highlighting their potential as powerful baselines for future research in self-supervised wireless channel representation learning.

Index Terms—Wireless Channel Modeling, Foundation Models, Transformer Architectures, Masked Autoencoder, Deep Learning.

I. INTRODUCTION

Large-scale self-supervised pretraining has transformed the fields of natural language processing and computer vision. This paradigm leverages diverse datasets and proxy objectives to learn broadly transferable representations, in contrast to traditional task-specific training approaches [2]–[4]. By decoupling feature learning from downstream tasks, it enables efficient, task-agnostic adaptation. Models following this two-stage strategy—computationally intensive pretraining followed by lightweight fine-tuning—are commonly referred to as *foundation models* [5].

A. Background and Motivation

Deep learning has demonstrated significant potential in wireless communications across a range of task-specific ap-

B. Guler and H. Jafarkhani are with the Center for Pervasive Communications and Computing, University of California, Irvine CA, USA. They were supported in part by the NSF Award CNS-2229467.

G. Geraci is with Nokia Standards and Universitat Pompeu Fabra, Spain. He was supported in part by the Spanish Research Agency grants PID2021-123990OB-I00, CEX2021-001195-M, and CNS2023-145384.

Some of the results in this paper have been submitted for publication in the Proc. IEEE GLOBECOM 2025 [1].

plications. For instance, deep neural networks have been employed for channel estimation and channel state information (CSI) feedback compression [6]–[11], end-to-end communication system design [12]–[14], and generative channel modeling [15]–[17]. Similarly, classification-based tasks such as beam management [18]–[20] and link blockage prediction [21], [22] can benefit from supervised deep learning techniques. These advances are also reflected in ongoing standardization efforts within 3GPP [23].

However, the prevailing paradigm in the wireless domain remains task-specific, often requiring ad-hoc architectures, labels, and retraining for each use case. In contrast, the notion of foundation models—pretrained on large-scale data using self-supervised objectives and adaptable across tasks—has yet to be fully embraced in the wireless domain. A limited but growing body of work has begun to explore task-agnostic self-supervised learning for wireless channel representation, with most efforts falling into two broad methodological categories: contrastive and reconstructive learning.

Contrastive learning typically utilizes encoder-only architectures to maximize representational similarity between augmented versions of identical data points (positive pairs) while minimizing similarity between distinct samples (negative pairs) [24], [25]. For example, one study treats CSI and channel impulse response (CIR) of the same wireless channel as positive pairs, maximizing their representational similarity in the embedding space [24]. A related investigation uses geospatial information by constructing a contrastive objective in which channels from identical geolocations serve as positive samples, while those from different locations serve as negative samples [25].

In parallel, *reconstructive methods* aim to predict or reconstruct masked portions of the input and can be categorized into three primary architectural patterns:

- 1) Decoder-only autoregressive models, such as GPT [3].
- 2) Encoder-decoder architectures, such as masked autoencoders (MAE) [26].
- 3) Encoder-only bidirectional models, such as BERT [2].

Among *decoder-only* models, one study fine-tunes a pre-trained GPT-2 language model with domain-specific adaptations for autoregressive channel prediction [27], while another extends this architecture to multimodal inputs, incorporating CSI and environmental metadata [28].

In terms of *encoder-decoder* approaches, the work in [29] employs a vision transformer-based autoencoder for masked

spectrogram prediction, demonstrating its effectiveness in human activity sensing and spectrogram segmentation tasks. Complementary research explores masked autoencoder pre-training for channel prediction [30], although it does not address transferability across different downstream tasks.

Encoder-only bidirectional models have received particular attention. In [31], a transformer encoder reconstructs masked CIR samples, although the model is described using GPT terminology despite the lack of an autoregressive decoder. A similar observation applies to [32], which also adopts masking-based reconstruction with an encoder-only architecture. The Large Wireless Model (LWM) represents a notable contribution, applying a masked modeling objective where random patches of multiple-input single-output (MISO) orthogonal frequency division multiplexing (OFDM) channel matrices are masked and subsequently reconstructed using a transformer encoder [33].

Despite these advancements, key limitations remain in current wireless foundation models. BERT-based architectures such as LWM [33] typically employ low masking ratios (e.g., 15%), which reduce the complexity of the pretraining task and may result in shallow or overspecialized feature representation. Furthermore, several approaches adapt BERT-style models by replacing the original cross-entropy loss with regression objectives tailored to continuous-valued wireless data, without thoroughly reassessing the implications for representation learning. These design choices can constrain the expressiveness and generalizability of the learned representations, ultimately limiting performance across diverse downstream wireless tasks.

More broadly, while contrastive and reconstructive approaches have each shown promise, they face fundamental limitations when applied in isolation to wireless channel modeling. Contrastive methods, for instance, are sensitive to the choice of positive and negative samples—poor sample selection can mislead the model, especially in wireless scenarios where channels may share subtle but significant similarities. These methods also typically require large batch sizes to provide a sufficient number of negative samples, increasing computational overhead [34], [35]. In contrast, reconstructive approaches tend to emphasize the accurate recovery of low-level statistical patterns, which may come at the expense of not learning the discriminative features necessary for downstream tasks such as beam selection. This produces representations that work well for regression tasks but may underperform in classification or decision-making scenarios that depend on fine-grained feature distinctions [36]. Combining both approaches in a multi-task framework addresses these weaknesses by enabling simultaneous learning of both structural and discriminative channel features.

B. Contribution and Summary of Results

In this paper, we introduce Wireless Masked Autoencoder (WiMAE), a pretrained transformer-based wireless channel foundation model based on the MAE framework. WiMAE directly addresses the limitations of prior reconstructive approaches by adopting an asymmetric encoder-decoder architecture that emphasizes abstraction over memorization. Inspired

by techniques in the vision domain [26], [37], WiMAE replaces the BERT-style regression loss with a structure that more effectively encourages the extraction of semantically meaningful features. Specifically, WiMAE’s encoder processes only the visible patches of the input, while a lightweight decoder reconstructs the masked portions. Unlike LWM’s shallow masking, WiMAE employs higher masking ratios, forcing the model to learn robust representations from limited observations and resulting in more transferable features across various wireless tasks.

Building upon the WiMAE foundation, we further enhance our approach by developing ContraWiMAE, which incorporates a contrastive learning objective alongside the reconstruction task in a unified multi-task framework. By warm-starting from pretrained WiMAE weights and generating positive pairs via the injection of additive white Gaussian noise (AWGN), ContraWiMAE contrasts these against negative samples drawn from different channel realizations. This enables the model to learn representations that are not only effective for reconstruction but also highly discriminative. The resulting hybrid approach significantly increases the linear separability of the learned embeddings, allowing simpler downstream models to achieve better performance without relying on complex architectures to compensate for representational weaknesses.

We evaluate the effectiveness of WiMAE and ContraWiMAE on two downstream tasks: cross-frequency beam selection and line-of-sight (LoS) detection. The beam selection task evaluates how well each encoding captures the channel’s detailed structure across antenna elements and subcarriers, while LoS detection measures the effectiveness of the extracted features as compact channel summaries. Key findings from our experiments include the following:

- WiMAE achieves optimal performance at a masking ratio of 0.6, outperforming competing baselines by up to 36.5% increase in accuracy in linear probing tasks.
- Increasing encoder depth yields diminishing returns beyond 12 layers, whereas deeper decoders improve representation quality without affecting inference latency.
- Higher-dimensional embeddings improve performance, especially for complex tasks; increasing the representation dimension from 32 to 64 leads to substantial gains with diminishing returns beyond 64.
- WiMAE demonstrates exceptional data efficiency, matching the performance of baseline models trained on complete datasets using only 1% of the training data.
- While complex downstream models help reduce performance gaps for other approaches, WiMAE shows minimal improvement from simple to complex models—indicating that it already produces near-optimal representations.
- The addition of a contrastive component in ContraWiMAE further enhances linear separability of the learned representations, leading to improved downstream performance, achieving up to 16.1% and 42.3% higher accuracy compared to WiMAE and other baselines, respectively.
- Warm-starting from pretrained WiMAE enables efficient training of ContraWiMAE without degrading the strong

reconstruction capabilities of the base model.

Relation to our prior work: This paper extends our preliminary work submitted to IEEE GLOBECOM 2025 [1]. While the conference version introduces the WiMAE architecture and demonstrates its promise for wireless channel representation learning via masked reconstruction, the present article offers substantial enhancements. Specifically: (i) we introduce ContraWiMAE, a novel multi-task extension that integrates contrastive learning to improve discriminability; (ii) we conduct a broader set of ablation studies and evaluate performance on two downstream tasks—beam selection and LoS detection—across a more exhaustive set of configurations, demonstrating significantly improved generalization, data efficiency, and linear separability of learned features; and (iii) we extract deeper insights into optimal architectural design, pretraining strategies, and fundamental relationships between model capacity, task complexity, and data efficiency.

Paper organization: The remainder of this paper is organized as follows. Section II describes the system model and problem formulation, together with the training objectives used for model optimization. Section III presents the WiMAE and ContraWiMAE architectures, detailing the preprocessing steps, encoder and decoder designs, and the integration of contrastive learning. Section IV outlines the methodology, including dataset generation, pretraining setup, and adaptations for downstream tasks. Section V reports and thoroughly analyzes the experimental results, highlighting their implications for wireless representation learning. Finally, Section VI concludes the paper.

II. SYSTEM MODEL AND PROBLEM FORMULATION

In this section, we describe the system model and problem formulation, along with the training objectives used for model optimization.

A. System Model

We consider a MISO-OFDM system with $N_f = 32$ subcarriers, 30 kHz subcarrier spacing, and a total system bandwidth of $B = 960$ kHz. The base station utilizes a uniform linear array (ULA) with $N_s = 32$ antennas and half-wavelength antenna spacing. The user equipment employs a single omnidirectional antenna. All antennas have isotropic radiation patterns and single polarization. The maximum number of propagation paths taken into account is set to 20 and Doppler effects are not considered. The frequency domain channel response for each symbol period is denoted as $\mathbf{H} \in \mathbb{C}^{N_s \times N_f}$ and is calculated between the base station and every user in a given scenario. To perform a fair comparison, our system model parameters are purposely chosen to match the configuration used in LWM [33].

B. Problem Formulation

We begin by formulating the basic WiMAE approach, then extend it to the ContraWiMAE framework that incorporates contrastive learning.

1) WiMAE: Masked Reconstruction Objective: We model the problem with a parameterized encoder-decoder pair (f_θ, g_ϕ) . Given a complex channel matrix $\mathbf{H} \in \mathbb{C}^{N_s \times N_f}$, our aim is to learn an efficient representation that captures the underlying structure with only partial observations.

Let \mathbf{M}' be a random masking operator drawn from a distribution $p(\mathbf{M}')$ that removes a portion of the information from \mathbf{H} , resulting in a partial observation $\mathbf{H}_m = \mathbf{M}'(\mathbf{H})$. Also, let $\overline{\mathbf{M}'}$ denote the complementary mask operation that selects only the masked portions.

We jointly optimize f_θ and g_ϕ to reconstruct the masked portions of \mathbf{H} from the visible portions \mathbf{H}_m by minimizing the reconstruction error in the minimum squared error (MSE) sense, focusing only on the masked regions. The loss function $\mathcal{L}_{\text{recon}}$ is defined as:

$$\mathcal{L}_{\text{recon}}(\theta, \phi) = \mathbb{E}_{\mathbf{H} \sim p(\mathbf{H}), \mathbf{M}' \sim p(\mathbf{M}')} \left[\|\overline{\mathbf{M}'}(\mathbf{H}) - \overline{\mathbf{M}'}(g_\phi(f_\theta(\mathbf{H}_m)))\|_F^2 \right], \quad (1)$$

where $\|\cdot\|_F$ denotes the Frobenius norm and $p(\mathbf{H})$ represents the distribution of channel matrices.

2) ContraWiMAE: Hybrid Reconstruction and Contrastive Learning: Building upon the WiMAE foundation, we enhance our approach by incorporating a contrastive learning objective alongside the reconstruction task in a multi-task framework.

Positive pair generation: For each channel matrix \mathbf{H}_i , we create a positive pair \mathbf{H}_i^+ by adding AWGN:

$$\mathbf{H}_i^+ \sim \mathcal{CN}(\mathbf{H}_i, \sigma^2 \mathbf{I}), \quad (2)$$

where σ^2 is a hyperparameter that controls the noise variance.

Contrastive learning objective: Let $\mathbf{H}_{i,m} = \mathbf{M}'(\mathbf{H}_i)$ and $\mathbf{H}_{i,m}^+ = \mathbf{M}'(\mathbf{H}_i^+)$ represent the masked versions of the original and augmented channel matrices, respectively. Let $\mathbf{z}_i = \mathcal{G}_\psi(f_\theta(\mathbf{H}_{i,m}))$ and $\mathbf{z}_i^+ = \mathcal{G}_\psi(f_\theta(\mathbf{H}_{i,m}^+))$ be the global embeddings derived by applying a nonlinear operator \mathcal{G}_ψ parameterized by ψ , which generates a low-dimensional representation of the encoder output. These embeddings are normalized to lie on a unit hypersphere for contrastive loss calculation. Inspired by Noise Contrastive Estimation [38] and following the InfoNCE approach [39], we formulate the contrastive objective as:

$$\mathcal{L}_{\text{contra}}(\theta, \psi) = -\mathbb{E}_{\mathbf{H}_i \sim p(\mathbf{H}), \mathbf{M}' \sim p(\mathbf{M}')} \left[\log \frac{\exp(\mathbf{z}_i \cdot \mathbf{z}_i^+ / \tau)}{\sum_{j=1, j \neq i}^{\mathcal{B}} \exp(\mathbf{z}_i \cdot \mathbf{z}_j / \tau)} \right], \quad (3)$$

where τ is a temperature parameter and \mathcal{B} is the batch size. This loss encourages the representation of a channel and its augmented version to be similar, while pushing apart representations of different channels in the same batch.

Combined multi-task objective: The combined training objective becomes:

$$\mathcal{L}(\theta, \phi, \psi) = \alpha \mathcal{L}_{\text{recon}}(\theta, \phi) + (1 - \alpha) \mathcal{L}_{\text{contra}}(\theta, \psi), \quad (4)$$

where α is a coefficient that trades off the reconstruction and contrastive objectives. The optimal parameters θ^* , ϕ^* , and ψ^* are obtained through:

$$(\theta^*, \phi^*, \psi^*) = \arg \min_{\theta, \phi, \psi} \mathcal{L}(\theta, \phi, \psi). \quad (5)$$

3) *Model Utilization Strategy*: While our primary focus is on the encoder f_θ , which produces the latent representations used for downstream tasks, both the decoder g_ϕ and the contrastive learning component \mathcal{G}_ψ play critical roles during training. The decoder enforces the reconstruction objective, encouraging the encoder to extract structurally informative features. The contrastive learning objective enhances the discriminative properties of these representations by pulling similar channel realizations closer in the embedding space while pushing dissimilar ones apart.

This multi-task training approach allows ContraWiMAE to simultaneously learn both structural and discriminative features, leading to more robust representations that generalize better across diverse wireless environments. During inference, the decoder is typically discarded when only the encoder's embeddings are needed (e.g., for downstream classification tasks). However, for tasks that require accurate signal reconstruction, the decoder remains relevant and can be retained to generate full outputs from partial observations.

III. PROPOSED ARCHITECTURE

In this section, we detail our proposed WiMAE and ContraWiMAE architectures to model the encoder-decoder pair (f_θ, g_ϕ) and the contrastive operator \mathcal{G}_ψ . The main building blocks are illustrated in Fig. 1, in which the contrastive head block, pictured with dashed lines, is the only difference between WiMAE and ContraWiMAE.

A. Preprocessing Operations

Partitioning: We partition the channel matrix $\mathbf{H} \in \mathbb{C}^{N_s \times N_f}$ into a set of non-overlapping patches, each with dimension $d_p = N_{p,s} \times N_{p,f}$. For simplicity, we assume that N_s is divisible by $N_{p,s}$ and N_f is divisible by $N_{p,f}$. This partitioning operation can be expressed as:

$$\mathbf{H}_p = \{\mathbf{p}_{i,j} \in \mathbb{C}^{N_{p,s} \times N_{p,f}} \mid 1 \leq i \leq \frac{N_s}{N_{p,s}}, 1 \leq j \leq \frac{N_f}{N_{p,f}}\}, \quad (6)$$

where $\mathbf{p}_{i,j}$ represents the patch at position (i, j) in the partitioned space.

Masking: We then apply a binary mask to these patches. Let $\mathbf{M} \in \{0, 1\}^{\frac{N_s}{N_{p,s}} \times \frac{N_f}{N_{p,f}}}$ be a mask that operates on patches, with entries $M_{i,j}$. We only retain visible patches, i.e., those for which $M_{i,j} = 1$, as follows:

$$\mathbf{H}_v = \{\mathbf{p}_{i,j} \mid \mathbf{p}_{i,j} \in \mathbf{H}_p, M_{i,j} = 1\}. \quad (7)$$

The mask ratio m_r , defined as the proportion of patches removed from processing, is calculated as:

$$m_r = 1 - \frac{1}{K} \sum_{i=1}^{\frac{N_s}{N_{p,s}}} \sum_{j=1}^{\frac{N_f}{N_{p,f}}} M_{i,j}, \quad (8)$$

where $K = \frac{N_s}{N_{p,s}} \cdot \frac{N_f}{N_{p,f}}$ is the total number of patches.

Vectorization: Next, we transform the visible patches into a sequence representation by ordering them based on their original positions in a row-major order. Let \mathbf{p}_v^k be the k -th visible patch in this ordering, with $1 \leq k \leq N_v$, where $N_v = (1 - m_r) \cdot K$ is the number of visible patches. To handle the complex-valued nature of the channel matrix, we separate each patch into its real and imaginary components $(\mathbf{p}_v^k)^r = \Re(\mathbf{p}_v^k)$ and $(\mathbf{p}_v^k)^i = \Im(\mathbf{p}_v^k)$, respectively, each with dimension $N_{p,s} \times N_{p,f}$. We flatten each component to a vector of length d_p and construct the visible patch sequence:

$$\mathbf{P}_v = [\text{vec}((\mathbf{p}_v^1)^r), \dots, \text{vec}((\mathbf{p}_v^{N_v})^r), \text{vec}((\mathbf{p}_v^1)^i), \dots, \text{vec}((\mathbf{p}_v^{N_v})^i)]^T \in \mathbb{R}^{2N_v \times d_p}, \quad (9)$$

where $\text{vec}(\cdot)$ denotes the vectorization operation that transforms a matrix into a column vector.

Linear projection: The sequence of visible patches \mathbf{P}_v is first processed through a linear projection layer, where a projection matrix $\mathbf{W}_0 \in \mathbb{R}^{d_p \times d_e}$ transforms each patch from its original dimension d_p to the hidden dimension of the encoder d_e :

$$\mathbf{Z}_0 = \mathbf{P}_v \mathbf{W}_0 + \mathbf{B}_0, \quad (10)$$

where $\mathbf{B}_0 \in \mathbb{R}^{2N_v \times d_e}$ is the bias matrix.

Positional encoding: To incorporate positional information, we maintain a set of positional encodings $\mathbf{PE}_e \in \mathbb{R}^{2K \times d_e}$ for all possible patch positions. The first K rows correspond to the positions of real components while the last K rows correspond to the positions of imaginary components. Let $\mathcal{I}_v \subset \{1, 2, \dots, 2K\}$ be the set of indices in the original patch sequence corresponding to visible patches (both real and imaginary components). We then add the subset of positional encodings corresponding to these visible patches as follows:

$$\mathbf{Z} = \mathbf{Z}_0 + \mathbf{PE}_e[\mathcal{I}_v, :], \quad (11)$$

where $\mathbf{PE}_e[\mathcal{I}_v, :]$ denotes the rows of \mathbf{PE}_e indexed by \mathcal{I}_v . This ensures that the network's input $\mathbf{Z} \in \mathbb{R}^{2N_v \times d_e}$ retains both the content information of the visible patches and their spatial positions within the original channel matrix.

B. Encoder Architecture

The encoder consists of L_{enc} transformer layers as described in what follows. Let $\mathbf{Z}^{(0)} = \mathbf{Z} \in \mathbb{R}^{2N_v \times d_e}$ be the initial input to the first layer.

Multi-head self-attention: Each layer $l \in \{1, 2, \dots, L_{\text{enc}}\}$ takes the output of the previous layer $\mathbf{Z}^{(l-1)}$ and processes it through multi-head self-attention (MHSA) with M_{enc} attention heads. For any layer, given an input \mathbf{Z}_{in} , the scaled dot-product attention in each head i is computed as $\text{head}_i = \mathbf{A}_i(\mathbf{Z}_{\text{in}} \mathbf{W}_i^Q + \mathbf{B}_i^Q)$, where \mathbf{A}_i is defined as

$$\mathbf{A}_i = \text{softmax} \left(\frac{(\mathbf{Z}_{\text{in}} \mathbf{W}_i^Q + \mathbf{B}_i^Q)(\mathbf{Z}_{\text{in}} \mathbf{W}_i^K + \mathbf{B}_i^K)^\top}{\sqrt{d_e/M_{\text{enc}}}} \right), \quad (12)$$

where $\mathbf{W}_i^Q, \mathbf{W}_i^K, \mathbf{W}_i^V \in \mathbb{R}^{d_e \times (d_e/M_{\text{enc}})}$ are the query, key, and value projection matrices, respectively, and $\mathbf{B}_i^Q, \mathbf{B}_i^K, \mathbf{B}_i^V \in \mathbb{R}^{2N_v \times (d_e/M_{\text{enc}})}$ are the corresponding bias matrices for the i -th head. Here, $\mathbf{A}_i \in \mathbb{R}^{2N_v \times 2N_v}$ represents the attention weights that capture the relationships between visible patches.

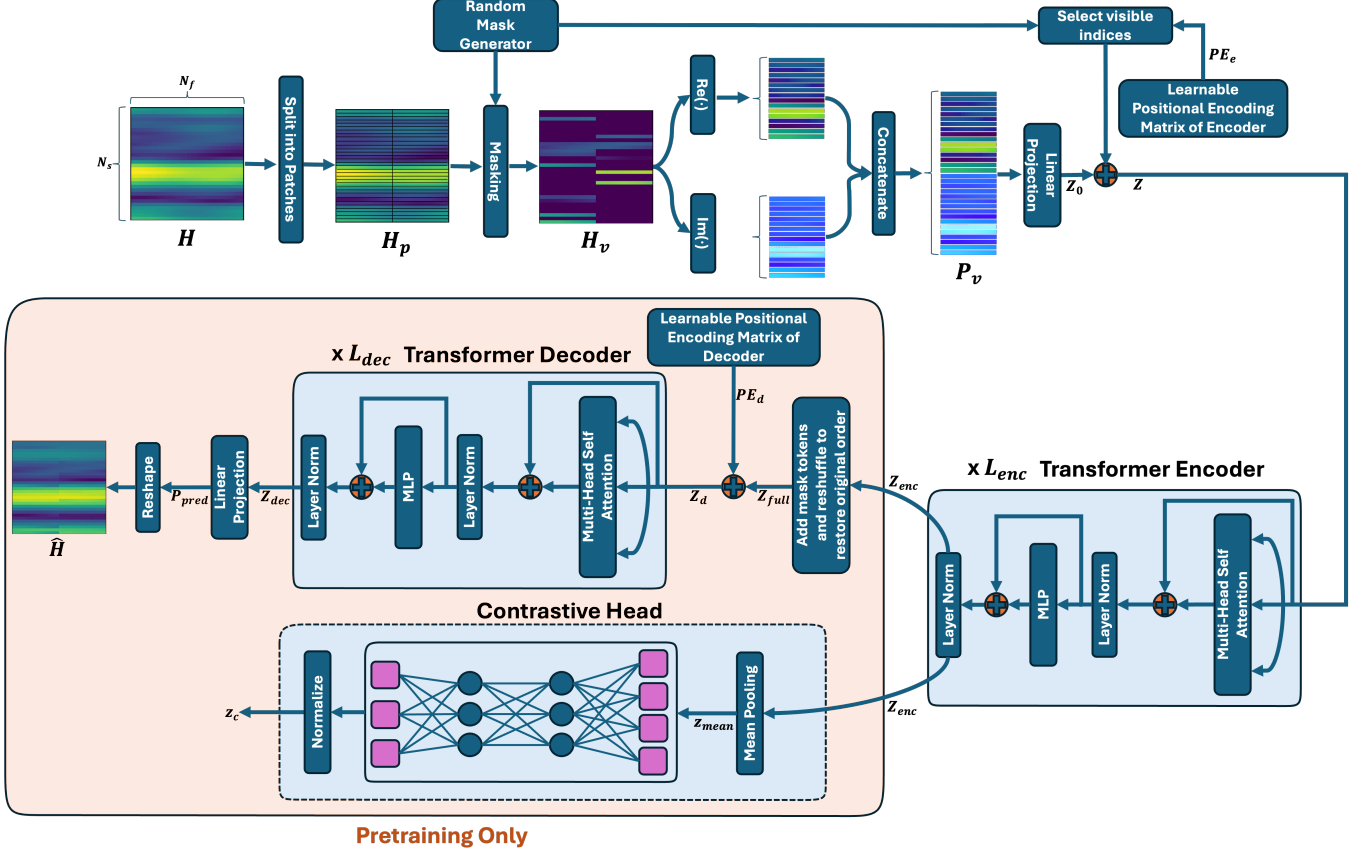


Fig. 1: Illustration of the WiMAE and ContraWiMAE architectures, detailing preprocessing steps, encoder processing, and decoding. WiMAE does not include the contrastive head block with dashed lines.

Multi-head concatenation and projection: The outputs from all M_{enc} attention heads are concatenated and linearly projected to obtain the final MHSA output:

$$\text{MHSA}(\mathbf{Z}_{in}) = \text{Concat}(\text{head}_1, \text{head}_2, \dots, \text{head}_{M_{enc}}) \mathbf{W}^O + \mathbf{B}^O, \quad (13)$$

where $\text{Concat}(\text{head}_1, \text{head}_2, \dots, \text{head}_{M_{enc}}) \in \mathbb{R}^{2N_v \times d_e}$ is the concatenation of all attention heads, $\mathbf{W}^O \in \mathbb{R}^{d_e \times d_e}$ is the output projection matrix, and $\mathbf{B}^O \in \mathbb{R}^{2N_v \times d_e}$ is the output bias.

Residual connection, layer normalization, and feed-forward network: The transformer layer applies residual connections, layer normalization (LN), and a multilayer perceptron (MLP):

$$\mathbf{Z}_{mid} = \text{LN}(\text{MHSA}(\mathbf{Z}_{in}) + \mathbf{Z}_{in}), \quad (14)$$

$$\mathbf{Z}_{out} = \text{LN}(\text{MLP}(\mathbf{Z}_{mid}) + \mathbf{Z}_{mid}), \quad (15)$$

where $\text{MLP}(\mathbf{Z}_{mid}) = \text{GELU}(\mathbf{Z}_{mid} \mathbf{W}_1 + \mathbf{B}_1) \mathbf{W}_2 + \mathbf{B}_2$ with $\mathbf{W}_1 \in \mathbb{R}^{d_e \times 2d_e}$ and $\mathbf{W}_2 \in \mathbb{R}^{2d_e \times d_e}$ as projection matrices, $\mathbf{B}_1 \in \mathbb{R}^{2N_v \times 2d_e}$ and $\mathbf{B}_2 \in \mathbb{R}^{2N_v \times d_e}$ as bias matrices, and GELU as the Gaussian Error Linear Unit activation function [40].

For each layer l , the output $\mathbf{Z}^{(l)} = \mathbf{Z}_{out}$ becomes the input to the next layer: $\mathbf{Z}_{in} = \mathbf{Z}^{(l)}$ for layer $l + 1$. After passing through all transformer layers, the final output $\mathbf{Z}^{(L_{enc})}$ becomes the encoder output $\mathbf{Z}_{enc} \in \mathbb{R}^{2N_v \times d_e}$ that captures the

contextual information from visible patches while maintaining their positional relationships.

C. Decoder Architecture

The decoder reconstructs the full channel matrix by processing both visible and masked patches. During pretraining, we first recover the complete patch sequence by restoring the original ordering of visible patches and inserting learnable mask tokens for the masked patches.

Restoring patch ordering and inserting learnable mask token: We initialize a sequence $\mathbf{Z}_{full} \in \mathbb{R}^{2K \times d_e}$ to represent all patches (both visible and masked) in their original positions. For each position i in the full sequence:

$$\mathbf{Z}_{full}[i] = \begin{cases} \mathbf{Z}_{enc}[j], & \text{if } i \in \mathcal{I}_v \text{ and } \mathcal{I}_v[j] = i \\ \mathbf{m}_{mask}, & \text{if } i \notin \mathcal{I}_v \end{cases} \quad (16)$$

where $\mathcal{I}_v[j]$ denotes the original position index of the j -th visible patch and $\mathbf{m}_{mask} \in \mathbb{R}^{d_e}$ is a shared, learnable mask token that is initialized as a zero vector but updated during training via backpropagation. This allows the model to learn an optimal representation for the masked tokens rather than being constrained to zeros.

Positional encoding: To incorporate positional information in the decoder, we add positional encodings $\mathbf{PE}_d \in \mathbb{R}^{2K \times d_e}$ directly to the sequence:

$$\mathbf{Z}_d = \mathbf{Z}_{full} + \mathbf{PE}_d, \quad (17)$$

where \mathbf{PE}_d represents the positional encodings corresponding to the original positions of all patches in the sequence.

Transformer layers: The decoder consists of L_{dec} transformer layers, each with M_{dec} attention heads. Each layer employs the same architecture as the encoder's transformer layers, with multi-head self-attention, residual connections, layer normalization, and multilayer perceptrons. The decoder uses the same dimension d_e as the encoder throughout its layers. The attention mechanism of the decoder allows both visible and masked patches to attend to each other, enabling information flow from visible patches to masked ones for reconstruction.

Final projection and reshaping: After passing through all transformer layers, the decoder produces output features $\mathbf{Z}_{dec} \in \mathbb{R}^{2K \times d_e}$ for all patches. These are then projected to the original patch dimension through a linear layer:

$$\mathbf{P}_{pred} = \mathbf{Z}_{dec} \mathbf{W}_{out} + \mathbf{B}_{out}, \quad (18)$$

where $\mathbf{W}_{out} \in \mathbb{R}^{d_e \times d_p}$ and $\mathbf{B}_{out} \in \mathbb{R}^{2K \times d_p}$ are the output projection matrix and bias matrix, respectively. The first K rows of \mathbf{P}_{pred} correspond to the real components, while the last K rows correspond to the imaginary components of the reconstructed patches. The predicted patches $\mathbf{P}_{pred} \in \mathbb{R}^{2K \times d_p}$ are then reshaped and recombined to form the reconstructed complex channel matrix $\hat{\mathbf{H}} \in \mathbb{C}^{N_s \times N_f}$.

D. ContraWiMAE Extension

Building upon the WiMAE architecture described above, we implement a contrastive learning extension that operates in parallel with the reconstruction pathway. This section details the specific implementation aspects of the contrastive component.

Global feature extraction: To obtain a compact representation of the encoder output $\mathbf{Z}_{enc} \in \mathbb{R}^{2N_v \times d_e}$, we first apply mean pooling across all visible patches to calculate $\mathbf{z}_{mean} \in \mathbb{R}^{d_e}$:

$$\mathbf{z}_{mean} = \frac{1}{2N_v} \sum_{i=1}^{2N_v} \mathbf{Z}_{enc}[i, :], \quad (19)$$

where $\mathbf{Z}_{enc}[i, :]$ is the i -th row of \mathbf{Z}_{enc} .

Projection to contrastive embeddings: \mathbf{z}_{mean} is projected to the contrastive embedding space with a two-layer MLP with a ReLU activation function, i.e.,

$$MLP^C(\mathbf{z}_{mean}) = \mathbf{W}_2^C \text{ReLU}(\mathbf{W}_1^C \mathbf{z}_{mean} + \mathbf{b}_1^C) + \mathbf{b}_2^C, \quad (20)$$

where $\mathbf{W}_1^C \in \mathbb{R}^{d_e \times 2d_c}$ and $\mathbf{W}_2^C \in \mathbb{R}^{2d_c \times d_c}$ are weight matrices, $\mathbf{b}_1^C \in \mathbb{R}^{2d_c}$ and $\mathbf{b}_2^C \in \mathbb{R}^{d_c}$ are bias terms, and d_c is the dimension of the contrastive embedding space. The final contrastive embedding $\mathbf{z}_c \in \mathbb{R}^{d_c}$ is obtained by applying L2 normalization to the projection output:

$$\mathbf{z}_c = \frac{MLP^C(\mathbf{z}_{mean})}{\|MLP^C(\mathbf{z}_{mean})\|_2} \in \mathbb{R}^{d_c}. \quad (21)$$

IV. METHODOLOGY

This section details the methodology used in our experimental evaluation of WiMAE and ContraWiMAE, including dataset generation, pretraining setup, and adaptations for downstream tasks. Through these experiments, we aim to demonstrate the effectiveness of our self-supervised learning approaches for wireless channel representation learning. A thorough discussion of the results is provided in Section V.

A. Dataset Generation

Using the DeepMIMO dataset [41], we generate 1.14M samples at 3.5 GHz operating frequency from 15 scenarios for pretraining. Each sample in the dataset corresponds to a channel for a distinct user and a single base station from one of the scenarios from: *Seattle, Los Angeles, Chicago, Houston, Phoenix, Philadelphia, Miami, Dallas, San Francisco, Austin, Columbus, New York, ASU Campus, Boston5G* and *O1*. We also generate a downstream task dataset with 14,840 samples from 6 unseen scenarios: *Denver, Fort Worth, Oklahoma, Indianapolis, Santa Clara, and San Diego*. Similar to the pretraining dataset, each scenario features one base station with uniformly distributed users. For a fair comparison, we match the configuration in both the pretraining and downstream datasets to the one in LWM [33].

B. Pretraining of WiMAE

We train WiMAE for 3,000 epochs with an 80/20 training/validation split on the pretraining dataset. We use the Adam optimizer with batch size of 3,072 and learning rate decaying from 3×10^{-4} to 3×10^{-6} with cosine decay. We explore different masking ratios $m_r \in \{0.45, 0.60, 0.75, 0.90\}$, network depths $L_{enc} \in \{6, 12, 18\}$ and $L_{dec} \in \{4, 8, 12\}$, encoding dimensions $d_e \in \{32, 64, 96, 128\}$, and patch configurations $(N_{p,s}, N_{p,f}) \in \{(1, 16), (4, 4)\}$, with fixed attention heads $M_{enc} = 16$ and $M_{dec} = 8$, as shown in Fig. 2.

The best reconstruction performance, illustrated in Fig. 3, is obtained with $(N_{p,s}, N_{p,f}) = (4, 4)$, achieving 29.14 dB SNR on the validation set. However, $(N_{p,s}, N_{p,f}) = (1, 16)$ leads to better performance in downstream tasks and is considered the default for the rest of the paper. Table I summarizes the pre-training configurations used for WiMAE and ContraWiMAE.

For comparisons with baseline models on downstream tasks, we set $m_r = 0.60$, $L_{enc} = 12$, $L_{dec} = 4$, $d_e = 64$, and $(N_{p,s}, N_{p,f}) = (1, 16)$. These choices result in 31% fewer encoder parameters and 7% fewer total parameters compared with LWM (see Table II). For LWM, we use publicly available pretrained weights and the code to generate its embeddings [33] without retraining or any modifications.

C. Pretraining of ContraWiMAE

We warm-start the encoder and decoder components of ContraWiMAE by copying the corresponding weights from WiMAE to preserve its reconstruction capability. We use the same learning rate schedule, optimizer, and batch size for continual pretraining of ContraWiMAE on the same pretraining dataset. To maximize the transferability of the reconstruction

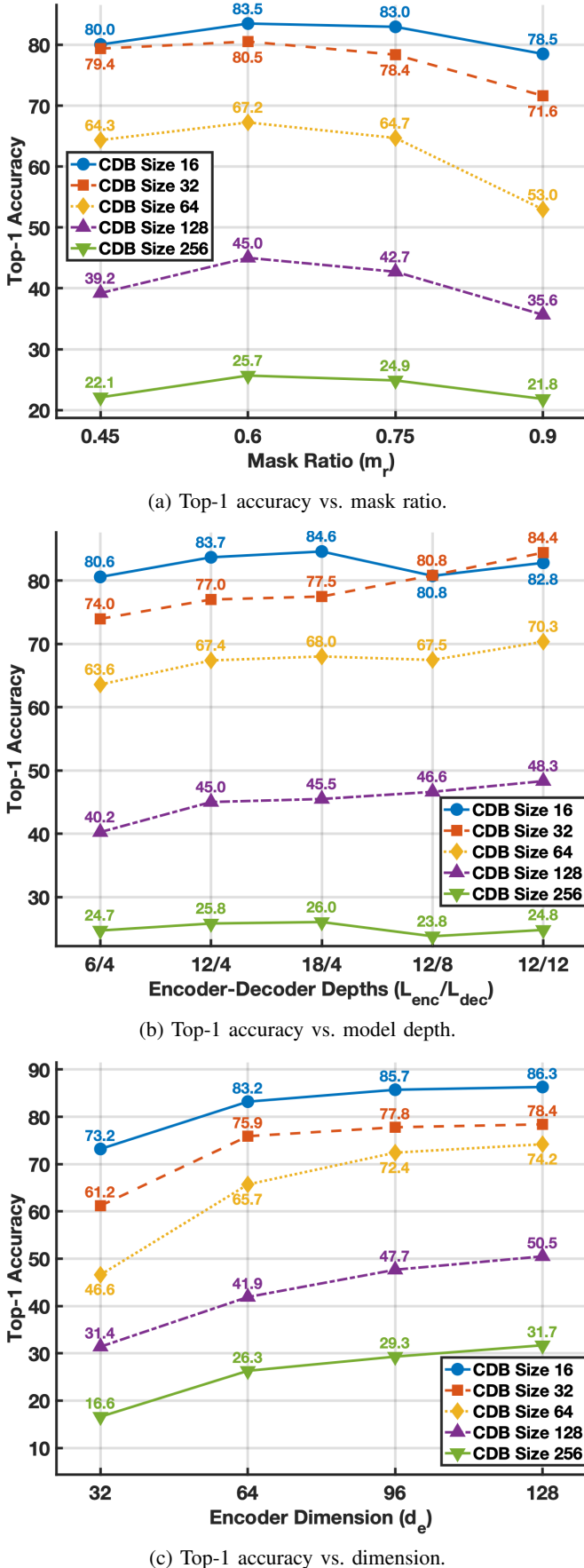


Fig. 2: Beam prediction performance for WiMAE with linear probing across different model parameters and codebook sizes.

capability, we use $m_r = 0.60$, $L_{\text{enc}} = 12$, $L_{\text{dec}} = 4$, $d_e = 64$, and $(N_{\text{p},\text{s}}, N_{\text{p},\text{f}}) = (1, 16)$, matching the parameters for WiMAE used in downstream task evaluations. We set the reconstructive and contrastive loss weights to $\alpha = 0.9$ and $1 - \alpha = 0.1$, respectively, using a temperature parameter $\tau = 0.1$. We also set the contrastive space dimension to $d_c = 64$ and uniformly sample the noise variance for positive pairs to achieve channel SNR values between 20 dB and 30 dB.

D. Downstream Task Adaptation

We evaluate WiMAE and ContraWiMAE on two downstream tasks: (i) cross-frequency beam selection and (ii) line-of-sight (LoS) detection, using 70/20/10 training/validation/test splits. The beam selection task evaluates how well each encoding captures the channel's detailed site-specific structure across antenna elements and subcarriers, while the LoS task measures the effectiveness of the extracted features as compact channel summaries.

1) *Cross-frequency Beam Selection*: The beam selection task predicts optimal mmWave beams at 28 GHz from 3.5 GHz channel data using predefined codebook sizes (CS) of 16, 32, 64, 128, and 256. This reduces the channel estimation overhead that is normally needed in beam management [42]

TABLE I: WiMAE and ContraWiMAE pretraining configurations.

Common parameters	Value
Training/validation split	80/20
Epochs	3,000
Batch size	3,072
Optimizer	Adam
Learning rate	3×10^{-4} with cosine decay
Attention heads	$M_{\text{enc}} = 16$, $M_{\text{dec}} = 8$
WiMAE	Value
Masking ratios m_r	{0.45, 0.60 , 0.75, 0.90}
Encoder depth L_{enc}	{6, 12 , 18}
Decoder depth L_{dec}	{4, 8, 12}
Embedding dim. d_e	{32, 64 , 96, 128}
Patch size $(N_{\text{p},\text{s}}, N_{\text{p},\text{f}})$	{(1, 16), (4, 4)}
ContraWiMAE	Value
Initialization	Warm-start from WiMAE
Loss coefficient in (4)	$\alpha = 0.9$
Contrastive temperature in (3)	$\tau = 0.1$
Contrastive dimension d_c	64
Positive pair generation	AWGN to achieve SNR $\in [20, 30]$ dB

Note: Boldface values are chosen for downstream task evaluation.

TABLE II: Parameter counts of different configurations.

Model	Encoder	Decoder	C. Head	Total
CWiMAE (12,4)	410,944	143,184	16,576	570,704
WiMAE (6,4)	210,112	143,184	-	353,296
WiMAE (12,4)	410,944	143,184	-	554,128
WiMAE (18,4)	611,776	143,184	-	754,960
WiMAE (12,8)	410,944	277,072	-	688,016
WiMAE (12,12)	410,944	410,960	-	821,904
LWM (12,-)	600,000	-	-	600,000

Note: CWiMAE = ContraWiMAE (contrastive learning variant). Model names show $(L_{\text{enc}}, L_{\text{dec}})$ where L_{enc} and L_{dec} are encoder and decoder layers. For WiMAE and CWiMAE: $M_{\text{enc}}=16$, $M_{\text{dec}}=8$, $d_e=64$.

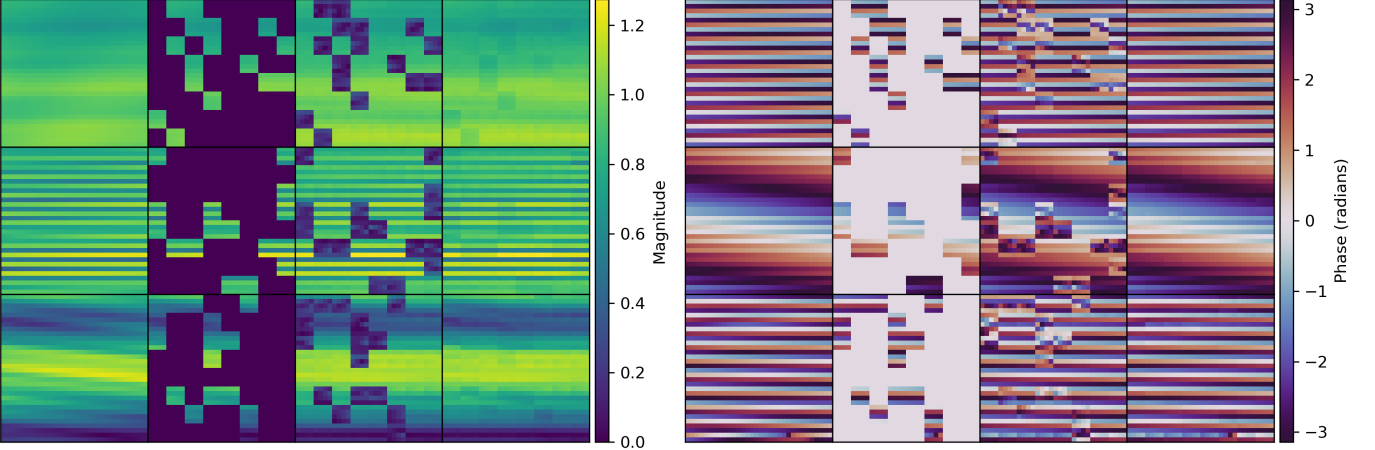


Fig. 3: Magnitude (left) and phase (right) reconstruction for WiMAE, obtained with patch size $(N_{p,s}, N_{p,f}) = (4, 4)$. Each row is a channel sample. Columns correspond to original, masked, reconstructed, and masked reconstructed channels.

while testing how well the learned representations capture cross-frequency propagation characteristics. We report top-1 and top-3 accuracy: top-1 accuracy measures the proportion of test samples where the predicted best beam matches the true optimal beam; top-3 accuracy extends this by considering a prediction correct if the true optimal beam is among the top three highest-scoring predicted beams. We compare models trained on WiMAE and ContraWiMAE embeddings with models trained on LWM embeddings and models trained on raw channel data without any representation learning (RAW), as summarized in Tables III and IV.

Downstream models: We employ several models for downstream evaluation.

- *Linear Probing:* This approach evaluates latent space linear separability by freezing encoder weights and training a linear classifier on top of the encoder to analyze how information can be directly extracted from the features without introducing nonlinearities [43]. As a lightweight and computationally efficient method, linear probing offers faster training and inference. To train a linear classifier, we minimize the cross-entropy loss using Adam optimizer with initial learning rate of 1×10^{-4} , exponential decay with $\gamma = 0.995$, and batch size of 512 until convergence.
- *ResNet Models:* We implement two residual network variants [44]. *ResNet-Wide*, the larger architecture with 57,000 parameters, features deeper layers with wider channel dimensions starting at 24 and expanding to 96 with a moderate dropout of 0.4. *ResNet-Slim*, the compact variant with 27,000 parameters, uses narrower channel dimensions starting at 16 and expanding to 64, reduced block counts and a lighter dropout of 0.3. Both architectures process encoded features through 1D convolutional layers with residual connections and batch normalization before classification with a fully connected network. For ResNet models, we use the same optimization parameters as linear probing since additional hyperparameter tuning does not lead to notable performance improvement.

2) *LoS Detection:* This task classifies if a channel exhibits the LoS condition, which can be crucial for adaptive modulation and coding, blockage prediction, and predictive handover. We report accuracy, F1 score, and area under the ROC curve (AUC), comparing the WiMAE and ContraWiMAE representations with the LWM baseline. In our comparison, we only employ linear probing since complex downstream models offer minimal additional improvement for this task. We use the CLS token for LWM and mean-pooled embeddings for WiMAE and ContraWiMAE. Although WiMAE and ContraWiMAE do not have a classification token like CLS, calculating the mean value across each patch encoding serves as a summary of the input. All experiments, shown in Table V, use Adam optimizer with a learning rate of 0.01 with exponential decay with $\gamma = 0.995$ and a batch size of 256.

V. ANALYSIS OF RESULTS

In this section, we examine in detail various model configurations and performance metrics across different downstream tasks and extract insights into optimal architectural design, pretraining strategies, and fundamental relationships between model capacity, task complexity, and data efficiency. Our comprehensive evaluation reveals both the strengths of our approaches and the nuanced interplay between different architectural choices.

A. Optimal Architectural Design of WiMAE

We begin by discussing the performance of WiMAE on the beam prediction downstream task, analyzing the impact of the masking ratio, the model depth, and the representation dimension. We also provide insights on the masked channel reconstruction, which is at the base of WiMAE’s pretraining stage.

Masking ratio: Fig. 2a reveals that for all codebook sizes considered, WiMAE’s performance peaks at a masking ratio of $m_r = 0.6$, with a notable decline at higher ratios. This suggests an optimal information density for these tasks where sufficient masking forces the model to learn meaningful representations

TABLE III: Top-1/top-3 accuracy for beam selection with linear probing.

Model	Codebook Size (CS)	Training Budget						
		1%	2%	5%	10%	25%	50%	100%
WiMAE	16	54.8/77.1	62.7/82.8	67.0/85.2	73.1/86.1	79.7/90.6	81.4/91.4	79.2/87.1
	32	39.9/58.2	47.2/66.0	55.3/74.6	61.7/74.9	72.9/82.5	74.8/81.0	72.4/76.6
	64	23.6/40.8	31.1/50.9	30.7/45.4	40.8/57.0	55.3/68.9	57.8/66.8	64.1/72.9
	128	12.7/22.0	16.9/28.0	17.5/30.2	23.6/35.4	31.5/45.3	35.6/47.6	39.8/46.6
	256	6.8/12.5	10.4/ 19.0	11.7/19.4	12.7/20.0	17.6/26.6	22.9/31.5	23.3/31.7
ContraWiMAE	16	54.2/76.4	65.3/85.9	73.8/89.1	76.2/87.9	81.3/92.5	83.0/91.6	85.0/92.6
	32	39.0/55.2	53.0/74.5	64.8/81.2	77.0/88.6	84.0/94.3	85.4/92.3	85.6/92.7
	64	24.9/41.2	32.5/51.8	44.7/66.7	55.0/74.6	67.7/84.4	75.8/88.3	74.7/82.0
	128	15.0/24.9	18.3/32.4	25.0/41.0	28.8/46.6	42.5/62.8	51.4/70.2	55.9/70.6
	256	7.9/13.5	10.5/18.7	14.7/24.1	17.3/27.2	22.5/35.4	27.4/41.5	31.3/45.2
LWM	16	17.5/27.5	23.6/35.3	19.0/32.2	26.0/36.9	36.8/48.5	39.6/47.9	42.7/53.6
	32	18.8/27.3	19.0/26.1	16.3/22.5	26.6/34.3	34.2/41.0	40.1/47.2	43.3/49.1
	64	14.8/20.7	18.9/25.8	11.8/16.4	21.3/27.2	27.8/35.0	33.0/39.7	36.7/42.6
	128	10.0/13.5	12.0/19.1	8.2/13.1	14.1/20.5	19.2/25.5	24.1/29.7	25.1/29.2
	256	5.3/8.0	8.6/12.9	6.0/10.4	8.3/12.2	11.6/17.1	13.7/18.8	13.7/19.2
RAW	16	31.6/41.5	33.9/42.8	34.0/43.7	38.2/45.8	38.8/46.3	39.8/44.4	41.7/48.0
	32	28.5/38.9	27.6/37.5	37.1/45.8	37.6/45.0	37.5/44.7	41.2/47.5	42.6/47.6
	64	19.4/29.2	25.2/36.2	29.3/41.6	32.0/42.8	34.6/43.1	37.1/44.5	36.5/42.2
	128	10.9/19.3	15.0/25.3	20.7/32.1	24.0/35.0	25.3/36.8	29.6/40.6	30.7/38.0
	256	6.2/10.9	9.9/15.8	11.5/19.1	15.0/24.9	18.7/26.1	20.0/31.5	22.7/31.7

Note: Boldface indicates the best result for each (CS, training budget) pair.

without compromising its ability to capture essential channel characteristics. At lower masking ratios (0.45), the pretraining task becomes less challenging, potentially leading to over-reliance on local correlations rather than learning global structural properties. In contrast, at extreme masking ratios (0.9), the reconstruction task approaches infeasibility, forcing the model to resort to generic patterns rather than capturing task-specific features.

Architecture depth: Fig. 2b demonstrates the complex relationship between model depth and performance. As the encoder depth increases from 6 to 12 layers, we observe consistent performance improvements across all codebook sizes. However, the marginal benefit diminishes beyond 12 layers, with 18-layer models showing minimal improvement. This suggests that moderate encoder depth effectively captures channel characteristics without excessive computation or potential overfitting. More interestingly, for a fixed 12-layer encoder, increasing the decoder depth from 4 to 8 and then to 12 layers provides substantial performance improvements. Since the decoder is discarded after pretraining, its added complexity does not affect inference latency. This asymmetric architecture—moderate encoder with deep decoder—reveals that a sophisticated decoding process provides a stronger learning signal that helps the encoder capture more nuanced channel features during training.

Representation dimension: Fig. 2c reveals a strong positive correlation between embedding dimension and performance, with patterns that vary by task complexity. Top-1 accuracy improves as the dimension increases from 32 to 128, with diminishing returns becoming apparent beyond 96. The most significant improvement occurs between dimensions 32 and 64, suggesting that this range is critical for adequately representing channel characteristics for the data under consideration. More

challenging tasks show less saturation at higher dimensions, indicating that complex discrimination tasks benefit more from increased representational capacity.

Reconstruction performance: Fig. 3 shows the reconstruction of both magnitude and phase information from heavily masked inputs using settings described in Section IV-B. As shown in the figure, WiMAE demonstrates impressive capability in capturing structural patterns rather than simply interpolating between known values. The reconstructions preserve characteristic fading patterns, spatial correlations across antenna elements, and coherent phase relationships between antenna elements and subcarriers. The transitions between visible and reconstructed regions are smooth, without boundary artifacts, demonstrating spatial coherence and the model’s ability to leverage global context. This quality of reconstruction with 60% masking suggests that WiMAE learns meaningful representations of the underlying channel physics rather than memorizing patterns, making it well-suited for fine-tuning on task-specific scenarios.

B. Comparison of WiMAE, ContraWiMAE, and Baselines

In this section, we compare the performance of WiMAE and ContraWiMAE to other baselines for the beam prediction and LoS detection downstream tasks. The full evaluation is reported in Table III, Table IV, and Table V, whereas Fig. 4 highlights the accuracy vs. training budget tradeoff obtained on beam selection for a codebook size of 32 and different downstream models.

Linear probing on beam selection: The results in Fig. 4a demonstrate WiMAE’s data efficiency. For codebook size 32, with only 1% training data, WiMAE achieves 39.9% top-1 accuracy, surpassing both LWM (18.8%) and raw models (28.5%). Notably, WiMAE with 5% training data outperforms

TABLE IV: Top-1/top-3 accuracy for beam selection with ResNet-Slim and ResNet-Wide.

Model	Codebook Size (CS)	Training Budget							
		ResNet-Slim				ResNet-Wide			
		10%	25%	50%	100%	10%	25%	50%	100%
WiMAE	16	33.0/60.9	67.8/86.2	74.0/90.2	79.9/93.0	64.3/83.2	78.6/92.6	81.9/94.7	84.0/96.0
	32	22.6/46.6	65.1/88.9	76.0/93.3	81.9/95.5	54.5/84.7	78.4/95.0	85.9/97.2	87.5/97.4
	64	2.8/7.9	32.8/61.7	63.9/90.6	76.0/95.3	28.1/58.0	64.7/90.6	74.6/95.3	81.0/97.2
	128	6.1/13.1	15.8/35.4	36.5/68.7	55.8/88.1	14.0/30.0	38.4/71.4	59.4/89.5	70.0/93.5
	256	1.1/2.9	8.0/16.4	17.3/ 40.0	37.7/73.0	8.0/15.8	18.2/40.2	30.8/66.0	49.9/85.6
ContraWiMAE	16	30.9/55.5	59.8/80.5	73.3/90.2	79.9/92.6	58.2/81.7	78.0/92.6	80.7/94.4	83.5/95.2
	32	17.9/39.8	46.4/74.8	74.7/94.1	84.5/96.4	47.3/71.6	79.7/96.0	85.7/97.3	87.7/97.5
	64	11.3/26.8	28.0/58.4	60.4/89.4	76.8/96.4	24.5/50.0	62.5/90.7	75.6/96.8	80.9/98.0
	128	5.0/12.1	14.5/31.1	34.0/65.0	60.2/91.9	13.6/27.6	33.3/64.6	59.2/92.3	69.3/95.6
	256	3.6/6.4	7.7/15.6	18.3/38.8	36.9/72.6	6.7/13.8	14.9/32.0	34.4/71.7	49.7/87.5
LWM	16	23.0/54.5	47.0/81.7	61.5/87.6	69.2/91.0	49.5/80.3	70.0/91.0	74.4/92.5	79.6/95.7
	32	12.3/32.6	33.1/67.1	55.3/86.1	71.3/94.2	33.8/65.0	67.3/90.1	76.8/97.0	81.3/96.8
	64	2.5/5.6	15.8/40.9	36.0/71.3	53.5/89.0	18.9/40.6	36.5/70.2	59.4/91.3	71.4/97.1
	128	0.7/1.9	6.8/16.1	13.7/35.3	36.9/74.9	7.8/18.6	19.6/41.8	34.6/71.0	54.6/90.6
	256	0.2/1.1	5.1/9.9	7.8/16.2	19.6/48.4	4.7/10.6	7.8/18.4	14.6/35.4	29.0/63.9
RAW	16	7.9/25.7	31.4/58.5	64.1/81.8	70.6/88.5	28.7/52.1	54.3/78.4	73.0/88.9	79.3/92.7
	32	4.0/13.1	27.2/54.7	55.4/79.0	72.7/91.6	24.3/43.6	50.0/76.3	72.9/92.9	86.1/97.0
	64	2.8/5.1	16.9/32.6	29.6/53.2	55.0/80.7	15.7/30.3	37.3/63.1	59.3/82.8	77.6/94.9
	128	1.6/4.3	8.1/18.4	20.6/38.8	45.0/76.4	8.7/17.9	24.0/43.6	44.8/72.8	66.4/90.8
	256	0.7/1.4	0.2/1.9	10.2/22.0	24.7/49.5	0.9/1.4	12.4/24.3	23.4/46.8	47.1/78.5

Note: Best results for slim and wide are bolded and both bolded and underlined, respectively.

TABLE V: Accuracy in the LoS detection task.

Training Budget (%)	LWM			WiMAE			ContraWiMAE		
	Accuracy	F1	AUC	Accuracy	F1	AUC	Accuracy	F1	AUC
1	0.929	0.941	0.981	0.931	0.944	0.980	0.931	0.944	0.981
2	0.946	0.957	0.985	0.941	0.953	0.983	0.941	0.953	0.983
5	0.926	0.942	0.973	0.944	0.955	0.985	0.949	0.959	0.987
10	0.943	0.955	0.987	0.947	0.958	0.989	0.950	0.960	0.989
25	0.946	0.957	0.988	0.957	0.965	0.992	0.951	0.960	0.990
50	0.950	0.960	0.989	0.958	0.966	0.992	0.956	0.965	0.992
100	0.948	0.959	0.989	0.960	0.968	0.993	0.959	0.967	0.992

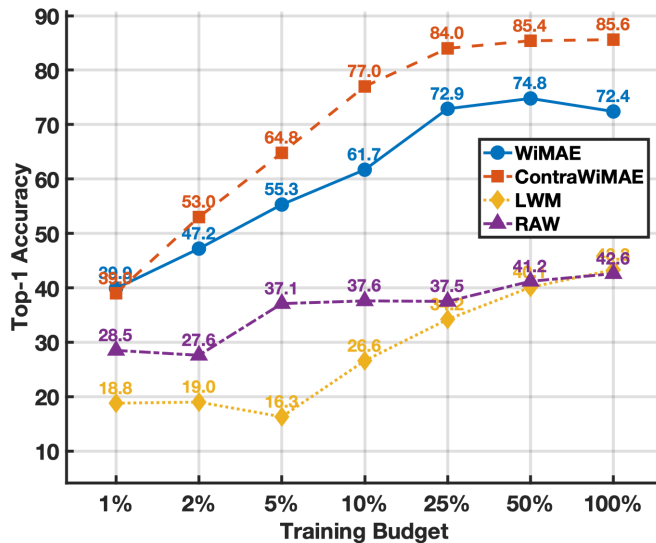
Note: Boldface indicates best result for each training budget.

LWM trained on the entire dataset, demonstrating superior feature extraction capabilities. The addition of contrastive learning in ContraWiMAE substantially enhances the linear separability of the encoded representations. With linear probing, as the training budget increases from 1% to 100%, ContraWiMAE demonstrates consistent performance scaling, with the advantage over WiMAE growing progressively larger. From Table III, we observe that this scaling effect becomes more pronounced with complex tasks (i.e., larger beam codebook sizes), where the contrastive objective promotes a more homogeneous utilization of the latent space, enabling clearer decision boundaries even as class complexity increases. This pattern suggests that contrastive learning enables the model to maintain discriminative power even as classification complexity increases, creating more linearly separable embeddings that preserve class distinctions without requiring complex downstream architectures.

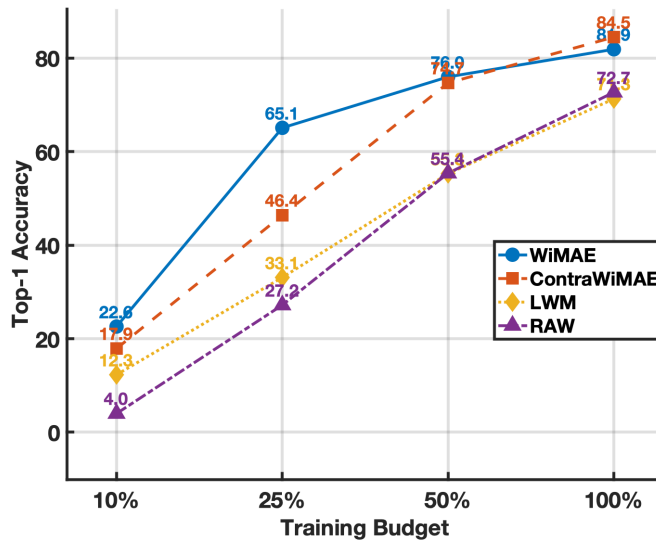
ResNet models on beam selection: Figs. 4b and 4c examine the top-1 beam selection accuracy with a codebook size of 32 when the downstream model is a ResNet-Slim and a ResNet-

Wide, respectively. While ContraWiMAE outperforms LWM by 42.3% with linear probing, this gap narrows to just 6.4% with ResNet-Wide, demonstrating how complex downstream architectures can offset weaker foundation representations. Table IV further shows that WiMAE and ContraWiMAE maintain their edge across configurations, especially in data-constrained scenarios. Notably, for a codebook size of 16 and 100% of the training budget, upgrading from linear probing to ResNet-Wide improves the top-1 accuracy for WiMAE by only 4.8%, while it improves LWM by 36.9%. This indicates that WiMAE’s representations are already well optimized. For complex tasks, increased downstream capacity benefits all models, though WiMAE maintains higher absolute performance.

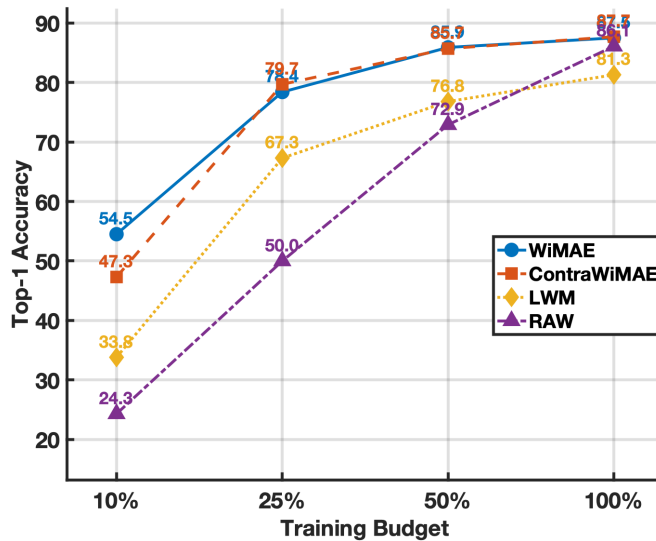
Linear probing on LoS detection: Table V examines the performance of different models for LoS detection. Both WiMAE and LWM exceed 92% accuracy even with just 1% training data, suggesting that LoS characteristics are more easily extractable compared to beam indices. WiMAE maintains a slight advantage with 100% training data (96.0% accuracy vs.



(a) Beam selection with linear probing, codebook size 32.



(b) Beam selection with ResNet-Slim, codebook size 32.



(c) Beam selection with ResNet-Wide, codebook size 32.

Fig. 4: Top-1 beam selection accuracy for a codebook size of 32 achieved by WiMAE/ContraWiMAE vs. baselines followed by (a) linear probing, (b) ResNet-Slim, and (c) ResNet-Wide.

94.8% for LWM). WiMAE shows consistent improvement as the training data increases, while LWM exhibits small fluctuations, suggesting that WiMAE provides more stable feature spaces. ContraWiMAE shows competitive performance with WiMAE, while consistently outperforming LWM, suggesting that introducing the contrastive objective does not hurt the encoder's ability to produce meaningful compact summary representations.

VI. CONCLUSION

In this paper, we introduced WiMAE, a transformer-based masked autoencoder specifically designed for wireless channel representation learning. By employing an asymmetric encoder-decoder architecture, high masking ratios, and moderate encoder depth, WiMAE strikes a balance between representational quality and computational efficiency. Our experiments showed that WiMAE consistently outperforms existing baselines across multiple downstream tasks, achieving particularly strong results under constrained data conditions. This efficiency is especially critical for practical wireless scenarios where labeled data is expensive or difficult to obtain.

To further enhance the quality of learned representations, we proposed ContraWiMAE, which extended WiMAE by incorporating a contrastive learning objective in a unified multi-task framework. Warm-starting from pretrained WiMAE weights and using additive noise to generate positive pairs, ContraWiMAE captures both structural and discriminative features of wireless channels. This hybrid approach further improves the linear separability of the learned embeddings, leading to enhanced downstream performance, especially with simple classifiers. Importantly, ContraWiMAE preserves the strong reconstruction performance of its base model, demonstrating that the two learning objectives can effectively complement each other.

Through extensive evaluation on realistic, previously unseen wireless scenarios, both WiMAE and ContraWiMAE exhibited strong transferability and robustness. WiMAE achieved optimal performance at a masking ratio of 0.6, with deeper decoders offering better representations without affecting inference latency. Larger embedding dimensions were found to be especially beneficial for complex tasks, and the data efficiency of both models enables high performance using as little as 1% of the training data employed by other baselines. Unlike other models that require complex downstream architectures to achieve good performance, WiMAE and ContraWiMAE produce representations that remain effective even with lightweight classifiers.

REFERENCES

- [1] B. Guler, G. Geraci, and H. Jafarkhani, "WiMAE: Wireless channel representation with masked autoencoder-based foundation model," submitted to *IEEE GLOBECOM 2025*.
- [2] J. Devlin, M.-W. Chang, K. Lee, and K. Toutanova, "BERT: Pre-training of deep bidirectional transformers for language understanding," in *Proc. NAACL-HLT*, 2019, pp. 4171–4186.
- [3] T. Brown, et al., "Language models are few-shot learners," in *NeurIPS*, vol. 33, 2020, pp. 1877–1901.
- [4] A. Dosovitskiy, et al., "An image is worth 16x16 words: Transformers for image recognition at scale," in *International Conference on Learning Representations*, 2021. [Online]. Available: <https://openreview.net/forum?id=YicbFdNTTy>

[5] R. Bommasani, et al., “On the opportunities and risks of foundation models,” 2022. [Online]. Available: <https://arxiv.org/abs/2108.07258>

[6] M. Soltani, V. Pourahmadi, A. Mirzaei, and H. Sheikhzadeh, “Deep learning-based channel estimation,” *IEEE Commun. Letters*, vol. 23, no. 4, pp. 652–655, 2019.

[7] C.-K. Wen, W.-T. Shih, and S. Jin, “Deep learning for massive MIMO CSI feedback,” *IEEE Wireless Commun. Letters*, vol. 7, no. 5, pp. 748–751, 2018.

[8] B. Guler and H. Jafarkhani, “AdaFortiTran: An adaptive transformer model for robust ofdm channel estimation,” in *IEEE International Conference on Communications (ICC)*, Montreal, Canada, June 2025, to appear.

[9] J. Park, F. Sohrabi, J. Du, and J. G. Andrews, “Self-nomination: Deep learning for decentralized CSI feedback reduction in MU-MIMO systems,” 2025. [Online]. Available: <https://arxiv.org/abs/2504.16351>

[10] J. Guo, C.-K. Wen, S. Jin, and G. Y. Li, “Convolutional neural network-based multiple-rate compressive sensing for massive MIMO CSI feedback: Design, simulation, and analysis,” *IEEE Transactions on Wireless Communications*, vol. 19, no. 4, pp. 2827–2840, 2020.

[11] J. Wang, X. Zhang, Z. Lu, J. Tan, and H. Zhang, “Practical deployment for deep learning-based CSI feedback systems: Generalization challenges and enabling techniques,” *IEEE Communications Magazine*, pp. 1–7, 2025.

[12] F. A. Aoudia and J. Hoydis, “End-to-end learning of communications systems without a channel model,” in *2018 52nd Asilomar Conference on Signals, Systems, and Computers*, 2018, pp. 298–303.

[13] J. Yang, W. Zhu, S. Sun, X. Li, X. Lin, and M. Tao, “Deep learning for joint design of pilot, channel feedback, and hybrid beamforming in FDD massive MIMO-OFDM systems,” *IEEE Communications Letters*, vol. 28, no. 2, pp. 313–317, 2024.

[14] J. Park, F. Sohrabi, A. Ghosh, and J. G. Andrews, “End-to-end deep learning for TDD MIMO systems in the 6G upper midbands,” *IEEE Transactions on Wireless Communications*, vol. 24, no. 3, pp. 2110–2125, 2025.

[15] W. Xia, S. Rangan, M. Mezzavilla, A. Lozano, G. Geraci, V. Semkin, and G. Loianno, “Generative neural network channel modeling for millimeter-wave UAV communication,” *IEEE Transactions on Wireless Communications*, vol. 21, no. 11, pp. 9417–9431, 2022.

[16] A. Giuliani, R. Nikbakht, G. Geraci, S. Kang, A. Lozano, and S. Rangan, “Spatially consistent air-to-ground channel modeling via generative neural networks,” *IEEE Wireless Communications Letters*, vol. 13, no. 4, pp. 1158–1162, 2024.

[17] T. Lee, J. Park, H. Kim, and J. G. Andrews, “Generating high dimensional user-specific wireless channels using diffusion models,” 2024. [Online]. Available: <https://arxiv.org/abs/2409.03924>

[18] Y. Heng and J. G. Andrews, “Grid-free MIMO beam alignment through site-specific deep learning,” *IEEE Transactions on Wireless Communications*, vol. 23, no. 2, pp. 908–921, 2024.

[19] K. Ma, Z. Wang, W. Tian, S. Chen, and L. Hanzo, “Deep learning for mmWave beam-management: State-of-the-art, opportunities and challenges,” *IEEE Wireless Communications*, vol. 30, no. 4, pp. 108–114, 2023.

[20] M. Qurratulain Khan, A. Gaber, P. Schulz, and G. Fettweis, “Machine learning for millimeter wave and terahertz beam management: A survey and open challenges,” *IEEE Access*, vol. 11, pp. 11 880–11 902, 2023.

[21] N. D. Cicco, S. Del Prete, S. Kodra, M. Barbiroli, F. Fuschini, E. M. Vitucci, V. Degli Esposti, and M. Tornatore, “Machine learning-based line-of-sight prediction in urban Manhattan-like environments,” in *2023 17th European Conference on Antennas and Propagation (EuCAP)*, 2023, pp. 1–5.

[22] S. Wu, M. Alrabeiah, C. Chakrabarti, and A. Alkhateeb, “Blockage prediction using wireless signatures: Deep learning enables real-world demonstration,” *IEEE Open Journal of the Communications Society*, vol. 3, pp. 776–796, 2022.

[23] 3GPP, “New SI: Study on Artificial Intelligence (AI)/Machine Learning (ML) for NR Air Interface,” 3rd Generation Partnership Project (3GPP), Technical Report TR 38.843, 2024, version 18.0.0.

[24] J. Jiang, W. Yu, Y. Li, Y. Gao, and S. Xu, “A MIMO wireless channel foundation model via CIR-CSI consistency,” 2025. [Online]. Available: <https://arxiv.org/abs/2502.11965>

[25] Z. Liu, J. Chen, Y. Xu, T. Ma, J. Liu, H. Zhou, and D. Niyato, “Leveraging self-supervised learning for MIMO-OFDM channel representation and generation,” 2024. [Online]. Available: <https://arxiv.org/abs/2407.07702>

[26] K. He, X. Chen, S. Xie, Y. Li, P. Dollár, and R. Girshick, “Masked autoencoders are scalable vision learners,” in *Proc. IEEE/CVF Conf. Computer Vision and Pattern Recognition (CVPR)*, 2022, pp. 16 000–16 009.

[27] B. Liu, X. Liu, S. Gao, X. Cheng, and L. Yang, “LLM4CP: Adapting large language models for channel prediction,” 2024. [Online]. Available: <https://arxiv.org/abs/2406.14440>

[28] L. Yu, L. Shi, J. Zhang, J. Wang, Z. Zhang, Y. Zhang, and G. Liu, “ChannelGPT: A large model to generate digital twin channel for 6G environment intelligence,” 2024. [Online]. Available: <https://arxiv.org/abs/2410.13379>

[29] A. Aboulfotouh, A. Eshaghbeigi, and H. Abou-Zeid, “Building 6G radio foundation models with transformer architectures,” 2024. [Online]. Available: <https://arxiv.org/abs/2411.09996>

[30] B. Liu, S. Gao, X. Liu, X. Cheng, and L. Yang, “WiFo: Wireless foundation model for channel prediction,” 2025. [Online]. Available: <https://arxiv.org/abs/2412.08908>

[31] J. Ott, J. Pirk, M. Stahlke, T. Feigl, and C. Mutschler, “Radio foundation models: Pre-training transformers for 5G-based indoor localization,” 2024. [Online]. Available: <https://arxiv.org/abs/2410.00617>

[32] T. Yang, P. Zhang, M. Zheng, Y. Shi, L. Jing, J. Huang, and N. Li, “WirelessGPT: A generative pre-trained multi-task learning framework for wireless communication,” 2025. [Online]. Available: <https://arxiv.org/abs/2502.06877>

[33] S. Alikhani, G. Charan, and A. Alkhateeb, “Large wireless model (LWM): A foundation model for wireless channels,” 2024. [Online]. Available: <https://arxiv.org/abs/2411.08872>

[34] Z. Cheng, H. Zhang, K. Li, S. Leng, Z. Hu, F. Wu, D. Zhao, X. Li, and L. Bing, “Breaking the memory barrier: Near infinite batch size scaling for contrastive loss,” 2024. [Online]. Available: <https://arxiv.org/abs/2410.17243>

[35] S. Ge, S. Mishra, C.-L. Li, H. Wang, and D. Jacobs, “Robust contrastive learning using negative samples with diminished semantics,” in *Advances in Neural Information Processing Systems*, M. Ranzato, A. Beygelzimer, Y. Dauphin, P. Liang, and J. W. Vaughan, Eds., vol. 34. Curran Associates, Inc., 2021, pp. 27 356–27 368.

[36] J. Lasserre, C. Bishop, and T. Minka, “Principled hybrids of generative and discriminative models,” in *2006 IEEE Computer Society Conference on Computer Vision and Pattern Recognition (CVPR’06)*, vol. 1, 2006, pp. 87–94.

[37] H. Bao, L. Dong, S. Piao, and F. Wei, “BEiT: BERT pre-training of image transformers,” 2022. [Online]. Available: <https://arxiv.org/abs/2106.08254>

[38] M. Gutmann and A. Hyvärinen, “Noise-contrastive estimation: A new estimation principle for unnormalized statistical models,” in *Proceedings of the Thirteenth International Conference on Artificial Intelligence and Statistics*, ser. Proceedings of Machine Learning Research, Y. W. Teh and M. Titterington, Eds., vol. 9. Chia Laguna Resort, Sardinia, Italy: PMLR, 13–15 May 2010, pp. 297–304. [Online]. Available: <https://proceedings.mlr.press/v9/gutmann10a.html>

[39] A. van den Oord, Y. Li, and O. Vinyals, “Representation learning with contrastive predictive coding,” 2019. [Online]. Available: <https://arxiv.org/abs/1807.03748>

[40] D. Hendrycks and K. Gimpel, “Gaussian error linear units (GELUs),” 2023. [Online]. Available: <https://arxiv.org/abs/1606.08415>

[41] A. Alkhateeb, “DeepMIMO: A generic deep learning dataset for millimeter wave and massive MIMO applications,” in *Proc. of Information Theory and Applications Workshop (ITA)*, San Diego, CA, Feb 2019, pp. 1–8.

[42] M. Giordani, M. Polese, A. Roy, D. Castor, and M. Zorzi, “A tutorial on beam management for 3GPP NR at mmWave frequencies,” *IEEE Communications Surveys & Tutorials*, vol. 21, no. 1, pp. 173–196, 2019.

[43] G. Alain and Y. Bengio, “Understanding intermediate layers using linear classifier probes,” 2018. [Online]. Available: <https://arxiv.org/abs/1610.01644>

[44] K. He, X. Zhang, S. Ren, and J. Sun, “Deep residual learning for image recognition,” in *Proceedings of the IEEE Conference on Computer Vision and Pattern Recognition (CVPR)*, June 2016.